Friedrich Schiller Universität Jena

PAF

Dissertation

High-Fluence Ion Beam Irradiation of Semiconductor Nanowires

Andreas Johannes

März 2015

Abstract

Hier alles Bla

Contents

1 Introduction

2 Background

This chapter will provide a general scientific context for this dissertation. First a general outline of energetic ion-solid interaction is given. Then the possibilities of simulating this ion-solid interaction are discussed with an emphasis on those effects that will be relevant to the experiment in this thesis.

2.1 Ion-solid interaction

Energy loss

An energetic ion impinging on a solid will lose its kinetic energy to the solid in a variety of processes. The stopping power S is well described for a large energy range by the Bethe (sometimes "Bethe-Bloch") formula derived using the Born approximation perturbation theory on the impact between the 'fast' ion and the 'slow' electrons in the solid:

$$S = \frac{dE}{dx} = -A \cdot \frac{\rho \, Z_2 \cdot Z_1^2}{\beta^2} \cdot \left[ln\Big(\frac{B \cdot \beta^2}{Z_2 \cdot (1 - \beta^2)} \Big) - \beta^2 \right], \qquad (2.1)$$

with A and B positive combinations of constants, ρ the density and Z_2 the atomic number of the target, Z_1 and $\beta = v/c$ the atomic number and relativistic velocity of the ion. Corrections to this formula are especially necessary for low ion energies, but in detail they are dependent on the
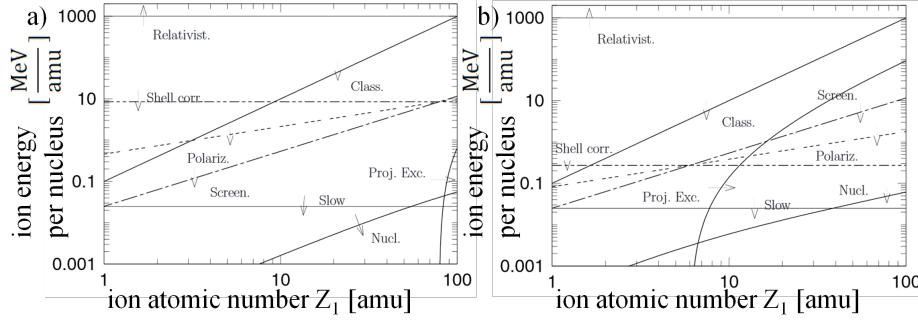
Figure 2.1: Illustration of the dominant effects on the stopping power for an ion of mass Z_1 and energy E in Au a) and C b). Adapted from [Sig04].

target composition, the ion energy and ion mass in a non-trivial way. Figure 2.1 and the following discussion illustrates stopping regimes and why corrections are required to the Bethe formula. It is adapted from [Sig04].

At high ion energies ($> 1\,GeV/amu$, labeled "Relativist.") highly relativistic effects have to be taken into account. At these energies we have, for example, Cherenkov radiation. Typically, nuclear reactions and resonances also occur at high ion energies. They may play a role at lower energies, especially for light ion-target combinations. However, as nuclear reactions may change the ion species, their cross sections are usually treated separately from the stopping power.

The horizontal line labeled "Shell corr." marks the Thomas-Fermi velocity ($Z_2^{2/3}v_0$) of the target electrons. The constant $v_0 = e^2/\hbar = 25\,keV/amu$ is the Bohr velocity. In the parameter-space below this line the ion is moving at speeds comparable to that of the electrons in the target. In the low energy area below the line labeled "Slow" ($25\,keV/amu$) the ion is traveling at speeds below the Bohr velocity of the target electrons. Here the ion velocity is only comparable to that of the valence electrons in the solid. Both these points mean that

the actual electron density distribution and chemical nature of the solid becomes relevant, which is of course not considered in the general Bethe formula. This makes a general and accurate theoretical prediction of electronic stopping impossible for low ion energies. Specific ion-target combinations require specific investigations.

Above the line showing the Thomas-Fermi velocity of the ion ($v = Z_1^{2/3} v_0$, "Screen.") the ion can be assumed to be stripped of all its electrons. Below, a screening function must consider the effective charge of the ion. Below the curve labeled "Proj. Ext." the ion (projectile) carries a comparable number of electrons to the target making excitation processes in the electronic configuration of the ion significant.

For ion velocities $v < (Z_1 Z_2)^{1/3} v_0$ (labeled "Polariz.") a higher order (Z_1^3) correction term to the Bethe formula becomes relevant due to the Barkas-Andersen effect. Below the line marked "Class." ($Z_1^2 \cdot 100 \, keV/amu$) classical Bohr orbits can be used for electrons around the ion, this is a *sufficient* criterion for the derivation of the Bethe formula not a *necessary* one.

Finally, not be confused with the nuclear reactions already mentioned, in the region marked "Nucl.", at low ion energies and for large ions, the interaction with the electronic system becomes weak. Here the contribution of the coulomb interaction between ion and individual target atoms as a whole become the main contribution to slowing the ion. This is called nuclear stopping in contrast to the electronic stopping discussed so far, as kinetic energy is transferred to the target nuclei, not just the electrons.

Those ion-solid interaction processes which are specific to the properties of the target material can be used to characterize the material. These methods are summarized as ion beam analysis (IBA). A confident and comprehensive review of the possibilities of IBA can be found in reference [JBB⁺12]. The effects that the ion irradiation has on the solid

will be discussed next by looking at the electronic and nuclear energy loss separately.

Discussion of electronic energy loss

Electronic stopping S_e "excites the electronic system". In the simplest case a target atom is ionized, followed by a host of effects such as characteristic X-ray emission and Auger electron emission associated with the relaxation of this excited state. Analogously, excitation in a semiconductor is associated with band to band, exciton etc. recombination. Detection of these emissions can be used for IBA. The luminescent and fluorescent relaxation mechanisms are, however, generally not very efficient. Most of the energy deposited in the electronic system will be turned into kinetic energy of electrons and subsequently converted to heat. This happens very locally on the nm scale of the electrons mean free path and thus also very quickly, within the order of ps.

The effects of such local heating on a solid are diverse. Defects and amorphous regions may either appear or disappear, depending on the material and its history. For large ion masses and energies (swift, heavy ions), the deposited energy density becomes large enough to form an "ion track" around the path of the ion. Ion tracks are a whole field of research outlined well by references [TDP92, MK97, WKW04]. Very large electronic losses have to be treated carefully as a large percentage of the electrons within the track are energized and some electrons also gain a significant amount of kinetic energy.

The energies used in this dissertation are in the order of $\approx 100\,keV$ with elements of mass $\approx 100\,amu$. The energy regime investigated in this dissertation is thus right at the bottom of the area plotted in figure 2.1. Electronic stopping is not dominant so that it is sufficient to treat the electronic energy loss as a local heat source.

Discussion of nuclear energy loss

The seemingly more straightforward process in the energetic ion-solid interaction is an elastic collision between the impinging ion and a target atom. Its first observation was in the famous Rutherford (Geiger–Marsden) experiment [Rut11] which was groundbreaking to understanding the structure of matter. Nuclear energy loss is caused by the kinetic energy which is transferred form the energetic ion onto an atom in the target. An impinging ion can transfer considerable energy to an atom, which in turn will collide with other lattice atoms, leading to the formation of a collision cascade. This displacement of atoms from their lattice position is the main contribution to irradiation damage and sputtering of the target.

The amorphization of crystalline semiconductors has been investigated extensively with a good review found in reference [WWS12]. The damage production depends a lot on the irradiated semi-conductor and on the density of the collision cascade caused by the irradiating ion. In general the defects produced by nuclear energy loss are Frenkel pairs. On further irradiation the Frenkel pairs can agglomerate to form extended defect clusters which initiate full amorphization. The fluence at which the material is amorphize is also highly temperature dependent as frenkel pairs can anneal at high implantation fluences. This can lead to an arbitrarily high amorphization fluence, if the annealing of defects is faster than their creation. A typical 'radiation hard' material is ZnO which does not amorphize at even at $10^{17}\,cm^{-2}\,Ar^+$ irradiation at $15\,K$ [WWS12]. An arbitrarily large amorphization threshold can also be obtained for Si irrdadiated with $300\,keV\,Ar^+$ at $300°\,C(\approx 600\,K)$ [PMB04].

In addition to the activation of defect recombination by increasing the 'global' temperature, an increased local temperature by the energy

deposited by the ion will also lead to 'dynamic annealing'. In a recent study [TVM+15] the dynamic annealing was enhanced by the simultaneous irradiation with $36\,MeV\,W$ a swift, heavy ion leading to predominantly electronic energy loss and $900\,keV\,I$ leading to large nuclear losses. Simultaneous irradiation lead to much less damage in the irradiated SiC than subsequent irradiation. The reduction of structure sizes also leads to larger dynamic annealing as there is less material into which the energy deposited by the ion can dissipate. This was shown in the Mn irradiation of $GaAs$ nanowires [Bor12, JHMR15] and could be used to improve the magnetic properties of the $GaAs:Mn$ nanowires [BMB+11, PKB+12, KPJ+13, PKJ+14].

A typical assumption in the theoretical treatment of nuclear energy loss is the binary collision approximation (BCA) for the ion and the target atoms. Under this assumption nuclear stopping is treated as a series of collisions between single particles. With the additional assumptions of 1) a spherically symmetric interaction potential and 2) the neglect of possible electronic effects (chemical binding) between the collision partners, the angular-momentum is conserved in the collision and the classical scattering-integrals can be solved.

The resulting trajectories of a $Si - Si$ collision at $10\,eV$ is plotted in figure 2.2. The large difference between the Moliére screened Coulomb potential and the $Si - Si$ potential derived by Dirac-Fock-Slater code is clearly visible. The former is a purely repulsive Coulomb interaction, while the latter includes an attractive interaction for large interatomic distances similar to the well known Lennard-Jones potential [Eck91]. For high energy collisions a "universal" ZBL potential based on Coulomb interaction is quite successful [ZLB85], however for low energy collisions a generalized formula cannot be accurate and specific potentials have to be developed for each combination of collision partners [Ded95, NRS97, ANNK02, ND08].
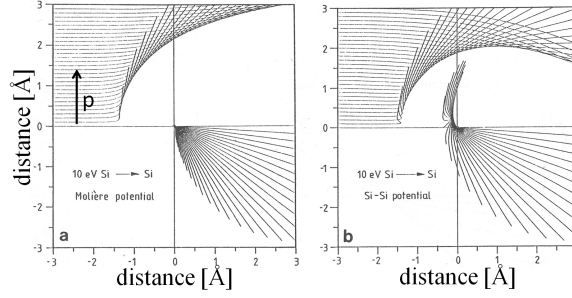
Figure 2.2: Trajectories of a $10\,eV$ $Si-Si$ collision for a) Moliére and b) $Si-Si$ potential. The trajectories end after the same elapsed time for each impact parameter p. Adapted from [Eck91].

In addition to this problem of finding the correct interaction potential for a collision, depending on the ion and the atomic structure of the irradiated material, the collision parameters relevant to low energy collisions are within the order of the inter-atomic distance of a few Å, see figure 2.2. The assumption, that this is still a binary collisions can thus no longer be valid. In conclusion, it has to be noted that similar to the electronic stopping case, the assumptions for a generalized treatment of nuclear stopping are well fulfilled for large ion energies, but lose their validity at low energies $\ll 1\,keV$.

Sputtering

A prominent role in this dissertation will be played by a special effect of nuclear energy loss arising when the path of a recoiled atom intersects the targets surface: sputtering. The foundation of sputter theory was laid by Sigmund [Sig69]. It is outlined in the following. The nuclear stopping of ions leads to the formation of highly branched collision cascades. Therefore, the majority of recoiled atoms is found at the end of the many branches. Because of this, the majority of sputtered particles has a low energy and thus a low range in the material [Tho68]. They

must thus originate from the surface of the target and the sputter yield, as the number of atoms sputtered per impinging ion, can be estimated by calculating the nuclear energy loss at the surface of the irradiated material and diving it by a factor to account for the probability of the atom leaving the solid.

The probability for the atom to leave the solid includes geometric considerations and the 'surface binding energy' (SBE). A possible model for an atom leaving a solid is that of a potential plateau with the height of the enthalpy of sublimation which has to be overcome by the atom approaching the surface. This equates the energy required for sputtering an atom to the thermal energy required for sublimation. For metals this is a good assumption, as the metallic bond is undirected and mediated by the electron gas. However, the SBE model for sputtering neglects all effects related to the directionality of the local binding forces experienced by the atom to be sputtered and the modification of the surface by repeated removal of atoms, which will be relevant in compounds with covalent and ionic bonds.

A reasonable assumption for the mean nuclear energy deposition distribution is be a Gaussian ellipsoid, with the center at the ion range and the longitudinal and lateral straggling naturally defining its extensions. This approach was used by Sigmund to arrive at a good explanation for the energy dependence of sputtering from flat surfaces. Starting a low energies, the sputter yield will initially increase with increasing energy, simply due to more energy being available. For further increasing energy, however, the ion range becomes larger, leading to a predominant deposition of the energy deeper inside the target, away from the surface. A maximum is thus found at energies where the ion range is in the order of the longitudinal straggling. The angle dependence of sputtering can also be explained by the increased deposition of energy near the surface for larger angles of incidence, as shown in figure 2.3.

Figure 2.3: Illustration of the Sigmund model of sputtering for irradiation of a bulk sample at an angle θ. The ion enters the target at the point O and deposits the nuclear energy as indicated by the oval contours. The energy deposited along the slanted surface BA is larger than that for the perpendicular surface $\tilde{B}\tilde{A}$ leading to increased sputtering for irradiation at an angle. Also the deposited energy and thus sputtering is not largest exactly at the point of incidence O, but further down at the point C. This is illustrated by the projection of the sputter yield 'S' onto the lateral dimension 'y'. Adapted from [Sig73].
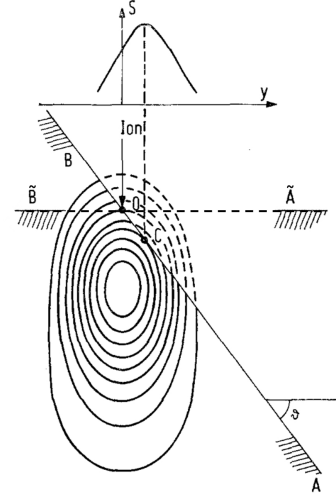
The Sigmund theory can also been applied to more complex surfaces. The Bradley-Harper theory of ripple formation on ion irradiated planes relies on the anisotropic sputtering predicted by the Sigmund model applied to a structured surface [Sig73, BH88]. The increased sputtering at a point (C) downstream from the point where the ion enters the target (O) leads to an enhancement of surface roughness.

The Sigmund theory predicts a maximum in sputtering where the ion range is comparable to the nanostructure diameter. This can be understood by considering sputtering for a fixed ion energy and varying diameter, illustrated in figure 2.4. At large diameters atoms can only be sputtered from the surface facing the ion beam. The sputter yield will still be larger than for a bulk sample as the local angle of irradiation is increased for non central impacts (A in figure 2.4). For decreasing diameters the curvature of the wires increases, further increasing the intersection area between the estimated energy distribution and the nanowire (B in figure 2.4). Once the diameter is in the order of the ion range, 'forward' sputtering along the direction of the ions initial path will become possible (C in figure 2.4). There is a maximum sputter yield for a radius
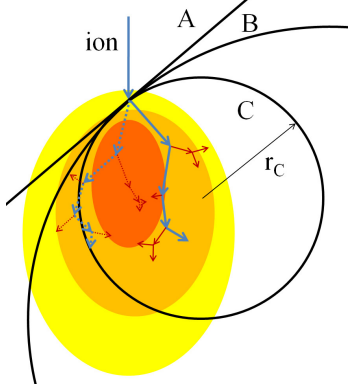
Figure 2.4: Illustration of the Sigmund model of sputtering for irradiation of a curved surface. For an infinite curvature radius (straight line A) a non-central impact is the same as irradiation at an angle, as shown in figure 2.3. For decreasing radii (B) the intersection between the colored energy distribution and the surface is increased. For small radii (r_C, C) forward sputtering appears. Two exemplary ion paths contributing to the colored average energy distribution are shown. The dashed path leaves and returns to the the smallest structure C.

comparable to the ion range, as the total surface area shrinks as $1/r^2$, reducing the sputter yield again for decreasing diameters.

This model is obviously limited, as the nuclear energy distribution is assumed to remain constant even if the target surface intersects it (dashed lines in figure 2.3). The maximum in the Gaussian ellipsoid approximation of the mean nuclear energy deposition is found where many of the branches of collision cascades overlap. A constant distribution wrongly includes those ion paths that would have left the nanostructure, as shown by the dashed ion trajectory in figure 2.4. The more detailed description of the process thus required is outlined in the following section on the simulation of ion-solid interaction.

2.2 Simulation of ion-solid interaction

In practice the theory of ion-solid interaction is implemented in simulation tools which allow the experimenter to predict experimental outcomes. The most frequent use for this is obtaining the energy dependence of the ion range by simulations and using that information to

decide which energy and fluence of irradiation is needed to obtain a desired doping concentration profile. On a more fundamental level, an experimentally observed behavior can be understood better by comparing it to various simulations to discern the dominating effects. The two main simulation approaches used to simulated the ion solid interaction are Monte-Carlo (MC) and Molecular Dynamic simulations (MD), both outlined in the following sections.

Monte-Carlo and the binary collision approximation

Monte-Carlo codes are simulation codes that use random numbers for simulations. After numerous simulations with different random outcomes, a statistical approximation of the likely outcome can be derived. With the BCA, the solid ion-interaction lends itself very well to MC simulation, as the evolution of a collision cascade can be simulated reiteratively by following the paths of the ion and all recoils. In the simplest case, three random numbers are needed per collision. The probability of a collision can be determined from the cross-sections determined by the interaction potential between the projectile and the atoms in the target. According to this probability, the first random number is used to determine the distance traveled in a straight line by the projectile. The particle's kinetic energy is reduced by the electronic energy loss according to the distance traveled. The underlying assumption here is that of a 'random material'. Crystal structure effects such as channeling are not reproduced by this simulation. Two further random numbers are used to determine the impact parameter and azimuthal angle. The trajectories of the projectile and target atom in the plane of impact after the impact are determined by this impact parameter, the interaction potential and the particle energy, as shown in chapter 2.1, figure 2.2.

12

Examples of simulation codes implementing this approach in static planar targets are SDTrimSP [BMS$^+$08], corteo [Sch08], COSIPO [Hau84] and, by far the most popular, SRIM [Zie12]. In TRIDYN [ME84] the target composition is 'dynamic', changing with the incorporation of ions and with selective sputtering of target atoms and the incorporated ions. It is clear from the discussion of chapter 2.1, figure 2.4 that the irradiation of a nanostructure can not be approximated well with a planar simulation. Therefore, the recently developed TRI3DYN [Mö14] and *iradina* [BR11] run a BCA MC simulation in a volume subdivided into rectangular voxels containing either vacuum or material to represent a three dimensional, structured target. TRI3DYN even includes dynamic composition and structural relaxation during the irradiation on a three dimensional simulation volume, but unfortunately it is not publicly available yet.

Several *iradina* simulation results will be discussed in this thesis, so the following points on the expected accuracy have to be made. The strong point of MC BCA simulations in general is that the direct simulation of the ion trajectories gives an accurate prediction of the distribution of the ions after irradiation, given the accuracy of the underlying theory of the energy loss discussed in the previous chapter. This can be expected to be upheld in the irradiation of nanowires. The concentration of incorporated ions is somewhat lower in nanowires than in bulk targets, as in a nanowire there are more ion paths that lead to the ions being scattered out of the nanowire, than there are in the irradiation of a bulk surface, see chapter 2.1, figure 2.4 and reference [Bor12].

The damage caused in the material by nuclear energy loss is a much more difficult prospect. The *iradina* code checks at each collision whether the target atom acquires more energy than the "displacement energy" which is a material specific parameter. If an atom has less than the displacement energy after a collision, it is assumed to remain bound in its

place and the energy is converted into lattice vibrations (= heat). Atoms with more energy are displaced, creating a Frenkel pair which is counted as an interstitial at the location the atom finally comes to rest and a vacancy at its point of origin. The displacement energy is experimentally accessible for crystalline materials by electron irradiation experiments in which the irradiating electron energy is in the order of MeV. From the electrons' impulse and mass the maximum transferred energy can be calculated. The defects produced as a function of electron energy can thus be used to determine a threshold energy for point defects, and this value is defined as the displacement energy. Firstly this not possible for amorphous materials, where point defects are ill-defined. Also, the number of Frenkel pairs this simulation creates is only an estimation at the *creation rate* of the defects. The critical role that defect mobility, agglomeration and annealing plays in ion damage is totally neglected [Nor14].

Even though *iradina* can implement an analytical description of a cylinder most of the simulations in this work were nevertheless performed on the voxel based simulation volume as this granted more freedom in the creation of the simulation volumes. The accuracy of the approximation of a curved surface, such as the surface of the cylindrical nanowires, is obviously dependent on the voxel size. Also, the surface and the surface of a cylinder is strictly smaller than its approximation by rectangular voxels and sputtering, as a surface effect, may be influenced. However, for voxel edges of $2\,nm$ and below only a negligible influence of the voxel size on the sputtering was found. In any case, the surface roughness of the nanowires during irradiation can be expected to be in this order of magnitude.

Molecular dynamic simulations

MD general: cite Alder, Nordlund+Kuronen

Relevant simulations in literature

Also recent investigations on sputtering of spherical [NSUM14] and cylindrical [UBNM15] nanostructures have found the Sigmund model to be a decent first approximation.

Furthermore, MC BCA simulations confirm and refine the prediction of radius dependent sputtering in spherical [NSUM14] and cylindrical [UBNM15] nanostructures by the Sigmund theory.

3 Experimental Methods

3.1 Nanowire synthesis

Nanowire synthesis can be categorized according to two approaches:
"bottom-up" and "top-down". The "bottom-up" approach relies on the
self-organized arrangement of matter using an inherent anisotropy in
the growth mechanism to create nanoscale structures. Depending on the
material, crystal quality, morphology, infrastructure requirements, the
quantity to be produced etc. there is a large variety of processes avail-
able for synthesis. For semiconductor nanowires the main approaches
developed are based on hydro-thermal, pyrolytic, vapor-transport, chem-
ical vapor deposition, laser ablation, metal organic vapor phase epitaxy
(MOVPE), molecular beam epitaxy (MBE) processes.

A very common mechanism to create the anisotropy required to get
the one dimensional growth of nanowires is the vapor-liquid-solid growth
(VLS) first described by Wagner and Ellis. The variety of processes listed
before are responsible to provide the 'vapor' of material for this growth
mechanism. With vapor transport the source material eg. ZnO is simply
evaporated in a typically inert atmosphere and transported within an
oven to the substrate by diffusion or gas flow. Chemical vapor deposition
uses reactive gases such as SiH_3 to provide the source material, in this
case Si in a temperature and pressure controlled oven. Similarly in

MOVPE a metal-organic gas is used as at least one of the sources. For example TMG (trimethylgallium) and AsH_3 to grow $GaAs$.

Although self-catalyzed growth has also been observed, the liquid part in VLS is typically played by a metal catalyst deposited on the growth substrate. The material in the vapor phase can collect in the catalyst droplet until the concentration is saturated. Preferential segregation of the nanowire material at the droplet-substrate interface leads to the growth of a wire. The size of the droplet can be used to control the diameter of the grown nanowire to some extent. ZnO [BMS+06, Sti08, Mü09, Ogr13], $GaAs$ [BDSS04, WDJ+09] and Si [LSH+08] nanowires investigated in this dissertation where grown with the VLS mechanism using vapor transport, MOVPE and chemical vapor deposition respectively. An epitaxial relation between the substrate and the nanowire material may be used to direct the growth. Typical nanowire diameters and lengths are $50 - 300\,nm$ and $> 10\,\mu m$ respectively.

Nanowires can also be synthesized "top-down". A "top-down" approach requires a predefined template which is used to control the desired morphology. The Si-nanowire arrays investigated within this dissertation were etched by reactive ion etching (RIE) through a circular, e-beam lithographically defined Ni hard-mask which set the nanowire diameter *cite NL* . With the "top-down" etching process it is possible to prepare nanowires with diameters varying from $50\,nm$ to $2\,\mu m$ with a height of $\approx 3\mu m$ on a single substrate for simultaneous irradiation.

Since the growth of nanowires was performed mainly by collaborators in Lund University ($GaAs$) and TU Vienna (Si) and is not part of the investigations reported here, the inclined reader is redirected to the the cited references for further details respective growth parameters and their investigation.

3.2 Modification

ROMEO

The ion irradiation for this dissertation was performed at the general purpose HVE implanter "ROMEO" at the IFK in Jena. It can provide an ion beam of virtually any element at energies of $10 - 380\,keV$. The beam passes a 90° selector magnet and can be swept with a frequency of kHz to homogeneously irradiate areas up to several tens of cm^2 with ion currents of up to $1\,mA$. For this work ion current densities were limited to $500\,nA/cm^2$ or $10^{16}\,ions/cm^2$ in $15\,min$. As previous work has shown that the irradiation of nanowires can bend the nanowires [BSL$^+$11, Bor12], a rotatable and heatable, tilted stage (RHT) was custom built [Noa14]. With it, bending of the nanowires that are upstanding on a substrate can be avoided as they are irradiated homogeneously from all sides at an angle of 45°. All the samples investigated in this thesis were rotated on the RHT and its preceding prototype sample stages during the irradiation.

FIB

Some sample preparation required a focused-ion-beam (FIB). FIBs are highly specialized ion accelerators where the main objective is to obtain a small ion beam focus. The most wide spread systems use a Ga^+ beam and acceleration voltages up to $30\,keV$. The main use for FIBs is to use the focused ion beam to sputter material extremely locally, making it a versatile tool for nano-machining. The FEI DualBeam Helios NanoLab 600i FIB system used for this dissertation is a scanning electron microscope (SEM) - FIB combination, so that the sample can be milled with the ion beam and investigated with the SEM. It also is equipped with a Pt-metal-organic-gas injection system. The Pt containing organic gas

can be cracked locally on the sample by the secondary electrons created by either the electron or the ion beam. The FIB system can thus deposit and mill structures on a nm scale. For the sample preparation in this thesis all Pt deposition was done with the electron beam. Most of the Pt is deposited near the impact point of the primary beam and the substrate, however typically a rather large 'halo' of minor Pt deposition can extend for a couple of μm.

3.3 Characterization

SEM

The morphological changes in the nanowires were characterized by high resolution SEM in the FEI DualBeam Helios NanoLab 600i focused-ion beam system. The spacial resolution of the SEM system is $\approx 2\,nm$. To quantify the sputtering, images of individual nanowires were made before and after ion irradiation. To find exactly the same place on the sample, a series of images with increasing magnification has to be made. Typically images were made at an angle of 45° to the substrate with the substrate aligned the same way before and after irradiation.

An semi-automated image analysis protocol was developed by Stefan Noack in his Master thesis [Noa14, **?**] to evaluate the SEM images of a large number of nanowires. It applies a (3x3) median filter to smoothe out some noise and a Gaussian unsharp mask with $\sigma = 1\,px$ and weighted at $60\,\%$ to resharpened the edges [San04]. An Otsu thareshold [Ots79] is applied to separate the lighter nanowire from the darker background. Next, open source particle analysis software is used to find the main body of the nanowire and turn the it upright, correcting for any marginal tilt remaining in the SEM images [SACF$^+$12, SPTS12]. Finally the sum of the gray-values in each line used to calculate the diameter at that

height along the nanowire axis. As the investigated nanowires showed a characteristic bulge at the base, this point can be used to align the height profiles of a single wire before and after irradiation.

EBSD

Electron back-scatter diffraction (EBSD) was used to identify whether nanowires remained crystalline after irradiation with a Carl Zeiss Auriga CrossBeam Workstation. EBSD can be measured with a large CCD detector in a SEM. The electron beam is focused on the sample at an arbitrary angle. Electrons are scattered from the sample lattice and the scattered electrons are detected by the CCD detector. Bragg diffraction along the crystal lattice planes produces a characteristic pattern of Kikuchi lines on the detector [Kik28, FH13] in crystalline samples. Amorphous or nano-crystalline samples show no pattern.

nano-XRF

The most experimentally advanced characterization method was X-ray fluorescence with a nano-focussed X-ray beam (nano-XRF) at the European Synchrotron Radiation Facility (ERSF), beamlines ID16b and ID13. Hard X-ray radiation excite the atoms within a radiated material to emit characteristic X-ray radiation. This X-ray fluorescence can be detected in an energy dispersive semiconductor detector and used to identify and quantify the elements in the sample. In principle the method is similar to the more wide-spread energy dispersive X-ray spectroscopy (EDX), where an electron beam is used to excite characteristic X-ray fluorescence. Very good lateral resolution can be obtained by having an EDX detector in an SEM. The advantage of using X-rays lies in the absence of Bremsstralung which high energy electrons in matter produce in addition to characteristic X-rays. In XRF there is thus a

much lower background and much lower concentrations of elements can be detected and quantified. Unlike normal X-ray tubes, synchrotron radiation is very brilliant, allowing it to be focused. The beamlines ID16b and ID13 were run at various energies above $16\,keV$ and a focus of typically $\approx 80\,nm$ and $\approx 250\,nm$ respectively. The nano-XRF thus allows for quantification of low concentrations with sufficient lateral resolution to resolve axial concentration gradients in a nanowire. Unfortunately, the resolution is not good enough to investigate radial distributions.

At both beamlines the nanowires are scanned under the fixed focal point of the X-ray beam with piezo-motors while the XRF spectra are collected with a Vortex EM silicon drift X-ray detector. The investigated Mn irradiated ZnO nanowires were deposited on TEM grids either randomly by 'imprinting' or individually by using the mico-manipulator in the FEI DualBeam FIB. Transferring individual wires requires some finesse, but it is possible to detach the ZnO nanowires from their substrate without the Ga FIB and to place them on the "lacey-carbon" TEM Grids without any additional Pt deposition. In this way SEM images before and after irradiation of the same wire investigated by nano-XRF are available.

The spectra used for quantification were obtained in multiple scans across a nanowire at regular intervals along the nanowire's length. As the XRF signal can be used to locate the nanowire, only the points near the nanowire were measured with a high integration time and a low step-with ($< \frac{1}{2}$ focal spot) to ensure a large number of counts ($> 10^5$ per scan) at reasonable measuring times.

nano-XRF quantification

The XRF-Spectra were evaluated using the open source PyMCA software package [SPC$^+$07]. The effects of self absorption and excitation can

be neglected, as the investigated nanowires are very thin compared to the absorption length of a couple of μm of hard X-rays in ZnO. However, the detector-sample distance is an unavoidable attenuation length in air, in which the X-ray absorption is dominated by Ar. As the element investigated, Mn, is relatively light, its characteristic X-ray emission at $K_{\alpha,Mn} = 5.9 \, keV$ suffers more absorption than the heavier Zn with $K_{\alpha,Zn} = 8.6 \, keV$. Thus absorption of the XRF signal in air has to be considered carefully in the fitting with PyMCA. The accuracy was double checked by measuring and quantifying trace elements in a calibration sample of bovine liver. In this way optimal fitting parameters were found for each beam-time and applied to the respective spectra in the PyMCA batch mode. Oxygen can not be quantified in these beamlines, as its XRF emission is totally attenuated by the air and a Si dead layer in the detector. The quantification of the Mn content in the ZnO nanowires thus relies on the assessment of the Mn/Zn ratio. It a decent approximation to assume that the ZnO remains stoichiometric even during the irradiation. The samples are irradiated in a chamber with a base pressure $\approx 10^{-6} \, mbar$, so according to the Hertz-Knudsen equation this will give a coverage of roughly one mono-layer or $10^{15} \, particles/cm^2s$. The maximum ion current density of $500 \, nA/cm^2s$ amounts to $10^{13} \, ions/cm^2s$, so that an unlikely amount of preferential sputtering would be required to deplete the oxygen out of the wires. In any case, the wires will be oxidized in the normal atmosphere post irradiation. The Mn/Zn ratio is thus a good proxy for the Mn concentration.

The quantification limit can be tested within PyMCA by finding an appropriate photon flux and nanowire interaction volume for a simulation to reproduce the XRF spectrum with the actually measured number of counts at $K_{\alpha,Zn}$. The Mn content in the simulated matrix can then be decreased until the minimum Mn content is found which gives a signal at $K_{\alpha,Mn}$ just above the actually measured noise level. In this way a

lower limit for the concentration resolution can be found at typically $0.1\,\%\,Mn/Zn$.

4 Summary and Outlook

check: Master Thesis Noack, Ogrisek, Conference proceding D. Sage, Rutherford, Nordlund

Bibliography

[ANNK02]   Karsten Albe, Kai Nordlund, Janne Nord, and Antti Kuronen. Modeling of compound semiconductors: Analytical bond-order potential for Ga, As, and GaAs. *Physical Review B*, 66(3):035205, July 2002.

[BDSS04]   M. Borgström, K. Deppert, L. Samuelson, and W. Seifert. Size- and shape-controlled GaAs nano-whiskers grown by MOVPE: a growth study. *Journal of Crystal Growth*, 260(1–2):18–22, January 2004.

[BH88]   R. Mark Bradley and James M. E. Harper. Theory of ripple topography induced by ion bombardment. *Journal of Vacuum Science & Technology A*, 6(4):2390–2395, July 1988.

[BMB+11]   Christian Borschel, Maria E. Messing, Magnus T. Borgstrom, Waldomiro Paschoal, Jesper Wallentin, Sandeep Kumar, Kilian Mergenthaler, Knut Deppert, Carlo M. Canali, Hakan Pettersson, Lars Samuelson, and Carsten Ronning. A New Route toward Semiconductor Nanospintronics: Highly Mn-Doped GaAs Nanowires Realized by Ion-Implantation under Dynamic Annealing Conditions. *Nano Letters*, 11(9):3935–3940, September 2011. WOS:000294790200073.

Bibliography

[BMS⁺06] C. Borchers, S. Müller, D. Stichtenoth, D. Schwen, and C. Ronning. Catalyst Nanostructure Interaction in the Growth of 1d ZnO Nanostructures. *The Journal of Physical Chemistry B*, 110(4):1656–1660, February 2006.

[BMS⁺08] Ivan Bizyukov, Andreas Mutzke, Ralf Schneider, Alexander M. Gigler, and Karl Krieger. Morphology and changes of elemental surface composition of tungsten bombarded with carbon ions. *Nuclear Instruments and Methods in Physics Research Section B: Beam Interactions with Materials and Atoms*, 266(9):1979–1986, May 2008. 00007.

[Bor12] Christian Borschel. *Ion-Solid Interaction in Semiconductor Nanowires*. PhD thesis, University Jena, Jena, 2012.

[BR11] C. Borschel and C. Ronning. Ion beam irradiation of nanostructures – A 3d Monte Carlo simulation code. *Nuclear Instruments and Methods in Physics Research Section B: Beam Interactions with Materials and Atoms*, 269(19):2133–2138, October 2011.

[BSL⁺11] Christian Borschel, Susann Spindler, Damiana Lerose, Arne Bochmann, Silke H. Christiansen, Sandor Nietzsche, Michael Oertel, and Carsten Ronning. Permanent bending and alignment of ZnO nanowires. *Nanotechnology*, 22(18):185307, May 2011. WOS:000288653300010.

[Ded95] Gv Dedkov. The Interatomic Interaction Potentials in Radiation Physics. *Physica Status Solidi a-Applications and Materials Science*, 149(2):453–513, June 1995. WOS:A1995RH61400001.

[Eck91]   Wolfgang Eckstein. *Computer Simulation of Ion-Solid Interactions.* Springer Berlin Heidelberg, Berlin, Heidelberg, 1991.

[FH13]   Brent Fultz and James Howe. *Transmission Electron Microscopy and Diffractometry of Materials.* Graduate Texts in Physics. Springer Berlin Heidelberg, Berlin, Heidelberg, 2013.

[Hau84]   M. Hautala. Nuclear stopping in polycrystalline materials: Range distributions and Doppler-shift attenuation analysis. *Physical Review B*, 30(9):5010–5018, November 1984. 00059.

[JBB+12]   C. Jeynes, M. J. Bailey, N. J. Bright, M. E. Christopher, G. W. Grime, B. N. Jones, V. V. Palitsin, and R. P. Webb. "Total IBA" - Where are we? *Nuclear Instruments & Methods in Physics Research Section B-Beam Interactions with Materials and Atoms*, 271:107–118, January 2012. WOS:000299986500018.

[JHMR15]   Andreas Johannes, Henry Holland-Moritz, and Carsten Ronning. Ion beam irradiation of nanostructures: sputtering, dopant incorporation, and dynamic annealing. *Semiconductor Science and Technology*, 30(3):033001, March 2015.

[Kik28]   Seishi Kikuchi. Diffraction of Cathode Rays by Mica. *Proceedings of the Imperial Academy*, 4(6):271–274, 1928.

[KPJ+13]   Sandeep Kumar, Waldomiro Paschoal, Andreas Johannes, Daniel Jacobsson, Christian Borschel, Anna Pertsova, Chih-Han Wang, Maw-Kuen Wu, Carlo M. Canali, Carsten Ronning, Lars Samuelson, and Håkan Pettersson. Magnetic Po-

Bibliography

larons and Large Negative Magnetoresistance in GaAs Nano-
wires Implanted with Mn Ions. *Nano Letters*, 13(11):5079–
5084, 2013.

[LSH+08]   A. Lugstein, M. Steinmair, Y. J. Hyun, G. Hauer, P. Pon-
gratz, and E. Bertagnolli. Pressure-induced orientation con-
trol of the growth of epitaxial silicon nanowires. *Nano Let-
ters*, 8(8):2310–2314, August 2008. WOS:000258440700034.

[Mü09]   Sven Müller. *Structural and optical impact of transition
metal implantation into zinc oxide single crystals and nano-
wires.* PhD thesis, Georg-August Universität Göttingen,
Göttingen, 2009.

[Mö14]   Wolfhard Möller. TRI3dyn – Collisional computer sim-
ulation of the dynamic evolution of 3-dimensional nano-
structures under ion irradiation. *Nuclear Instruments and
Methods in Physics Research Section B: Beam Interactions
with Materials and Atoms*, 322:23–33, March 2014. 00001.

[ME84]   W. Möller and W. Eckstein. Tridyn — A TRIM simula-
tion code including dynamic composition changes. *Nuclear
Instruments and Methods in Physics Research Section B:
Beam Interactions with Materials and Atoms*, 2(1–3):814–
818, March 1984.

[MK97]   Antonio Miotello and Roger Kelly. Revisiting the thermal-
spike concept in ion-surface interactions. *Nuclear Instru-
ments and Methods in Physics Research Section B: Beam In-
teractions with Materials and Atoms*, 122(3):458–469, Febru-
ary 1997.

28

[ND08]   Kai Nordlund and Sergei L. Dudarev. Interatomic potentials
           for simulating radiation damage effects in metals. *Comptes
           Rendus Physique*, 9(3–4):343–352, April 2008.

[Noa14]   Stefan Noack. *Sputter Effects of Silicon Nanowires under
           Ion Bombardment.* University Jena, Master Thesis, 2014.

[Nor14]   Kai Nordlund. Correction to the Kinchin-Phase damage
           equation to account for athermal defect recombination and
           ion beam mixing: arc-dpa and rpa. Leuven, September 2014.

[NRS97]   K. Nordlund, N. Runeberg, and D. Sundholm. Repulsive
           interatomic potentials calculated using Hartree-Fock and
           density-functional theory methods. *Nuclear Instruments &
           Methods in Physics Research Section B-Beam Interactions
           with Materials and Atoms*, 132(1):45–54, October 1997.
           WOS:A1997YF32200007.

[NSUM14]   Maureen L. Nietiadi, Luis Sandoval, Herbert M. Urbassek,
           and Wolfhard Möller. Sputtering of Si nanospheres. *Physical
           Review B*, 90(4):045417, July 2014.

[Ogr13]   Matthias Ogrisek. *Kontrolliertes Wachstum von Zinkoxid
           und Vanadium(IV)-oxid Nanodrähten.* University Jena,
           Master Thesis, 2013.

[Ots79]   NOBUYUKI Otsu. A Threshold Selection Method from
           Gray-Level Histograms. *IEEE Transactions on Systems,
           Man, and Cybernetics*, 9(1):62–66, 1979.

[PKB+12]   Waldomiro Paschoal, Sandeep Kumar, Christian Borschel,
           Phillip Wu, Carlo M. Canali, Carsten Ronning, Lars Samuel-
           son, and Hakan Pettersson. Hopping Conduction in Mn Ion-

Bibliography

Implanted GaAs Nanowires. *Nano Letters*, 12(9):4838–4842, September 2012. WOS:000308576000069.

[PKJ⁺14]   W. Paschoal, Sandeep Kumar, D. Jacobsson, A. Johannes, V. Jain, C. M. Canali, A. Pertsova, C. Ronning, K. A. Dick, L. Samuelson, and H. Pettersson. Magnetoresistance in Mn ion-implanted GaAs:Zn nanowires. *Applied Physics Letters*, 104(15):153112, April 2014. WOS:000335145200060.

[PMB04]   Lourdes Pelaz, Luis A. Marqués, and Juan Barbolla. Ion-beam-induced amorphization and recrystallization in silicon. *Journal of Applied Physics*, 96(11):5947–5976, December 2004.

[Rut11]   E Rutherford. The scattering of alpha and beta particles by matter and the structure of the atom. *Philosophical Magazine Series 6*, 21(125):669–688, May 1911.

[SACF⁺12]   Johannes Schindelin, Ignacio Arganda-Carreras, Erwin Frise, Verena Kaynig, Mark Longair, Tobias Pietzsch, Stephan Preibisch, Curtis Rueden, Stephan Saalfeld, Benjamin Schmid, Jean-Yves Tinevez, Daniel James White, Volker Hartenstein, Kevin Eliceiri, Pavel Tomancak, and Albert Cardona. Fiji: an open-source platform for biological-image analysis. *Nature Methods*, 9(7):676–682, June 2012.

[San04]   B Sankur. Survey over image thresholding techniques and quantitative performance evaluation. *Journal of Electronic Imaging*, 13(1):146, January 2004.

[Sch08]   François Schiettekatte. Fast Monte Carlo for ion beam analysis simulations. *Nuclear Instruments and Methods in Physics*

Research Section B: Beam Interactions with Materials and Atoms, 266(8):1880–1885, April 2008.

[Sig69]   Peter Sigmund. Theory of Sputtering. I. Sputtering Yield of Amorphous and Polycrystalline Targets. *Physical Review*, 184(2):383–416, August 1969. 03204.

[Sig73]   Peter Sigmund. A mechanism of surface micro-roughening by ion bombardment. *Journal of Materials Science*, 8(11):1545–1553, November 1973.

[Sig04]   Peter Sigmund, editor. *Stopping of Heavy Ions*, volume 204 of *Springer Tracts in Modern Physics*. Springer Berlin Heidelberg, Berlin, Heidelberg, 2004.

[SPC⁺07]   V. A. Solé, E. Papillon, M. Cotte, Ph. Walter, and J. Susini. A multiplatform code for the analysis of energy-dispersive X-ray fluorescence spectra. *Spectrochimica Acta Part B: Atomic Spectroscopy*, 62(1):63–68, January 2007.

[SPTS12]   Daniel Sage, D. Prodanov, J.-Y. Tinevez, and J. Schindelin. ImageJ User & Developer Conference (IUDC'12). 2012.

[Sti08]   Daniel Stichtenoth. *Dimensionseffekte in Halbleiternanodrähten*. PhD thesis, Georg-August Universität Götingen, Göttingen, 2008.

[TDP92]   M. Toulemonde, C. Dufour, and E. Paumier. Transient thermal process after a high-energy heavy-ion irradiation of amorphous metals and semiconductors. *Physical Review B*, 46(22):14362–14369, December 1992.

Bibliography

[Tho68]   Mw Thompson. Energy Spectrum of Ejected Atoms During High Energy Sputtering of Gold. *Philosophical Magazine*, 18(152):377–&, 1968. WOS:A1968B525400015.

[TVM+15]   Lionel Thome, Gihan Velisa, Sandrine Miro, Aurelien Debelle, Frederico Garrido, Gael Sattonnay, Stamatis Mylonas, Patrick Trocellier, and Yves Serruys. Recovery effects due to the interaction between nuclear and electronic energy losses in SiC irradiated with a dual-ion beam. *Journal of Applied Physics*, 117(10):105901, March 2015. WOS:000351442900074.

[UBNM15]   Herbert M. Urbassek, R. Mark Bradley, Maureen L. Nietiadi, and Wolfhard Möller. Sputter yield of curved surfaces. *Physical Review B*, 91(16):165418, April 2015.

[WDJ+09]   Brent A. Wacaser, Kimberly A. Dick, Jonas Johansson, Magnus T. Borgström, Knut Deppert, and Lars Samuelson. Preferential Interface Nucleation: An Expansion of the VLS Growth Mechanism for Nanowires. *Advanced Materials*, 21(2):153–165, January 2009.

[WKW04]   W. Wesch, A. Kamarou, and E. Wendler. Effect of high electronic energy deposition in semiconductors. *Nuclear Instruments & Methods in Physics Research Section B-Beam Interactions with Materials and Atoms*, 225(1-2):111–128, August 2004. WOS:000223792600010.

[WWS12]   W. Wesch, E. Wendler, and C. S. Schnohr. Damage evolution and amorphization in semiconductors under ion irradiation. *Nuclear Instruments and Methods in Physics Research*

Section B: Beam Interactions with Materials and Atoms, 277:58–69, April 2012. 00009.

[Zie12]   James Ziegler. *SRIM - The Stopping and Range of Ions in Matter.* February 2012.

[ZLB85]   J. F. (James F.) Ziegler, U. Littmark, and J. P. Biersack. *The stopping and range of ions in solids / J.F. Ziegler, J.P. Biersack, U. Littmark.* The Stopping and ranges of ions in matter ; v. 1. Pergamon, New York, 1985. Includes index. Bibliography: p. 308-315.